



Supplementary Information for
Multiple Flat Bands and Topological Hofstadter Butterfly in Twisted
Bilayer Graphene Close to the Second Magic Angle

Xiaobo Lu^{1†*}, Biao Lian^{2†}, Gaurav Chaudhary^{3,8†}, Benjamin A. Piot⁴, Giulio Romagnoli⁵, Kenji Watanabe⁶, Takashi Taniguchi⁶, Martino Poggio⁵, Allan H. MacDonald³, B. Andrei Bernevig⁷ and Dmitri K. Efetov^{1*}

¹ICFO - Institut de Ciències Fòniques, The Barcelona Institute of Science and Technology, Castelldefels, Barcelona 08860, Spain.

²Princeton Center for Theoretical Science, Princeton University, Princeton, New Jersey 08544, USA.

³Department of Physics, University of Texas at Austin, Austin, Texas 78712, USA.

⁴Université Grenoble Alpes, Laboratoire National des Champs Magnétiques Intenses, UPS-INSA-EMFL-CNRS-LNCMI, 38000 Grenoble, France

⁵Department of Physics, University of Basel, Basel 4056, Switzerland

⁶National Institute for Materials Science, 1-1 Namiki, Tsukuba 305-0044, Japan

⁷Department of Physics, Princeton University, Princeton, New Jersey 08544, USA

⁸Present address: Material Science Division, Argonne National Lab, Lemont, Illinois 60439, USA

*corresponding author: Xiaobo Lu, Dmitri K. Efetov

Email: xiaolu@phys.ethz.ch, dmitri.efetov@icfo.eu

This PDF file includes:

Supplementary text
Figures S1 to S14
SI References

Supplementary Information Text

1. Device information

We have measured devices with four different twist angles [D1-1 (0.45°), D1-2 (0.44°), D2 (0.38°) and D3 (0.34°)]. Fig. S1 shows optical microscope images of corresponding stacks and devices.

2. Gap opening at low magnetic field

Fig. S2 shows the temperature dependent R_{xx} vs. n measured at different magnetic field B_{\perp} . At zero magnetic field, all integer filling states exhibit a metallic behavior (Fig. S2A). Interestingly, at finite B_{\perp} , these states start becoming thermally activated, showing an insulating behavior (Fig. S2B-D). As shown in Fig. S3, the gap values are extracted by fitting $R_{xx} \sim \exp(\Delta/2kT)$ temperature activated behavior for all integer filling states. We further demonstrate the evolution of gaps with magnetic field B_{\perp} (Fig. S4) for these state. All these gaps increase when magnetic field B_{\perp} becomes large until quantum Hall regime starts to dominate the transport. To understand the magnetic field induced metal-insulator transition in tBLG better, we have further measured the device D1-1 with tilted magnetic field (Fig. S5). By comparing Fig. S5a and Fig. S5B, we have found that the resistivity of all integer filling states is only sensitive to the perpendicular component of magnetic field. Our results indicate that it is orbital effect instead of spin that leads to the gap opening here. This is consistent with the fact that the Dirac nodes at a certain integer filling (if semi-metallic) are protected by a $C_{2z}T$ symmetry which does not act on spin (where T is the spinless time-reversal operator which does not act on spin) (1). Since in-plane field only acts on spin, it cannot gap out the Dirac nodes in the semimetallic case. In the case where the system has no Dirac nodes but a small gap, a small B_{\perp} would produce Landau levels and enlarge the gap, while an in-plane field shifts the spin up and down (pointing in-plane) bands oppositely and thus generically reduces the gap, which is also consistent with our experimental observation

3. Hofstadter butterfly of tBLG with different angles

In Fig. S7-8, we demonstrate magneto-transport results of three more devices (D2 0.38°, D3 0.34° and D1-2 0.44°). Similar with the spectrum shown in Fig. 2 in main text, all samples we have measured exhibit robust unbounded and connected features in Hofstadter spectrum. As shown continuous extension of LLs from the CNP to higher moiré bands shows a clear evidence of nontrivial band topology of tBLG, which otherwise would be obstructed. Similar with D1-1 shown in main text, (4, 0), (-4, 0), (8, 1) and (-8, -1) LL gaps are still dominant in the Hofstadter spectrum and crossing several moiré bands, giving an unbounded and connected Hofstadter butterfly in all devices. Some $C = 0$ gaps also reappear in magnetic field, i.e. the (0, 0) gap starts to appear when the magnetic flux through one moiré unit cell is close to half quantized value $\phi_0/2$, whereas (0, ± 1) gaps reappear when the magnetic flux is above ϕ_0 . We find that (0, ± 1) gaps in all measured samples are interrupted by (± 4 , 0) gaps that are emerging from the CNP. Moreover, (0, ± 2) gaps in device D2 and (0, -2) in device D1-2 also reappear above ϕ_0 and are further interrupted by (± 4 , 0) gaps.

4. Hofstadter butterfly of fragile topology

As demonstrated in Ref (2), the Hofstadter butterfly of the lowest two fragile topological bands of the single-valley tBLG continuum model (see SM Sec. 6 for definition) is always connected with the Hofstadter spectra of the higher bands at certain nonzero magnetic fluxes per moiré unit cell, which can be understood as the fingerprint of the fragile topology (this is specifically true for the tBLG continuum model here; see the last paragraph of this section for a brief discussion of generic $C_{2z}T$ fragile topology models). For large enough twist angles ($> 2^\circ$), the perturbation analysis in Ref (2) shows that the Dirac helicity $\eta = 2$ at each graphene valley (which gives the fragile topology of the lowest two tBLG moiré bands) leads to two Chern gaps ($\pm 4, 0$) (counting the 4-fold spin-valley degeneracy) extending from the lowest two moiré bands to all the higher bands, which interrupts all the moiré band gaps (0, s) at nonzero integer fillings $s = n/n_s$. As a result, the Hofstadter

butterflies of all the moiré bands are connected together at nonzero magnetic fields. Numerical calculations in Ref (2) show that in a vast range of twist angle and relaxation parameter (see SM Sec. 6 for definition) including the parameters for the tBLG samples in our experiment, the Hofstadter spectrum of the lowest two moiré bands is connected with the spectrum of the higher bands at nonzero magnetic fluxes no larger than $\phi/\phi_0 = 1$.

Here we also show in Fig. S9 (replotted from Ref (2)) the calculated Hofstadter butterfly for the ten-band tight-binding model for tBLG (single spin and single valley) proposed by Ref (3), which faithfully characterize the fragile topology of the tBLG continuum model. In Fig. S9, we have multiplied all the Chern numbers of the Hofstadter gaps of the tight-binding model by 4, accounting for the 4-fold spin-valley degeneracy. One can clearly see that the Hofstadter spectrum of the lowest two bands is connected with the higher Hofstadter spectra at $\phi = \phi_0$, and the first moiré band gap $(0, \pm 1)$ are interrupted by the Chern gaps $(\pm 4, 0)$ from the CNP which extend all the way to higher bands.

We note that depending on twist angle and the relaxation parameter, the lowest two moiré bands are not always gapped from the higher bands at zero magnetic field (in the absence of interactions). When there is no gap from the higher bands at zero magnetic field (for example, in the range of angles we study in this paper), the fragile topology of the lowest two moiré bands is in principle ill-defined. However, it is shown in previous work (1) that in all the tBLG parameter (twist angle) range where the lowest two moiré bands are gapped from the higher bands, the lowest two moiré bands are fragile topological. This shows that the gap closing and reopening between the lowest two moiré bands and the higher moiré bands in the entire tBLG parameter range do not alter the fragile topology of tBLG, and the Dirac helicity $\eta = 2$ of each graphene valley at the CNP remains robust. As a result, for angles where the lowest two moiré bands are gapless with the higher bands, we find the fingerprint of the fragile topology, that the Hofstadter spectra of the lowest two moiré bands and the higher moiré bands are connected at nonzero magnetic field, remains unchanged.

We also note that, in a generic symmetry analysis, a model with two fragile topological bands protected by $C_{2z}T$ symmetry could have their Hofstadter butterfly disconnected with that of the other bands, due to the T symmetry breaking in the zero field model (4). However, the disconnection of the Hofstadter butterfly requires a large enough T symmetry breaking; the $C_{2x}C_{2z}T$ symmetry of the graphene model at any magnetic field also allows for Weyl points on the y-momentum axis. In particular, for the TBG continuum model, by both theoretical and numerical analyses, it is shown in Ref (2) that the Hofstadter butterfly connection between the lowest two fragile topological bands and the higher bands (in the range of nonzero magnetic fluxes including infinity) is stable for all the twist angles and relaxation parameters $0 \leq u_0 \leq 1$.

5. Bandstructure of 0.45° tBLG and Hartree-Fock calculation

We perform a self-consistent Hartree-Fock (HF) calculation for the continuum model to examine the effects of Coulomb interaction between electrons at integer moiré fillings $n = Nn_s$ ($N \in \mathbb{Z}$) at zero magnetic field. We take the Coulomb interaction

$$H_I = \frac{1}{2} \sum_{\alpha, \beta, q, k, k'} \frac{V(q)}{A_{tot}} c_{\alpha, k+q}^\dagger c_{\alpha, k} c_{\beta, k'-q}^\dagger c_{\beta, k'}$$

where $V(q) = 2\pi e^2(1 - \delta_{q,0})/\epsilon q$ is the Fourier transform of Coulomb interaction $e^2/\epsilon r$ subtracting the background charge, A_{tot} is the total area of the system. $c_{\alpha, k}$ is the annihilation operator of the Dirac electron of the monolayer graphene at momentum \mathbf{k} (the plane wave basis), and α is a shorthand notation for multiple indices: the sublattice $a = A, B$, layer $l = 1, 2$, spin $s = \uparrow, \downarrow$ and graphene valley $\eta = K, K'$ indices (see also SM Sec. 6). The electron eigenstates are given by the single-particle mean-field Hartree-Fock Hamiltonian

$$H = H_0 + \Sigma_H + \Sigma_F,$$

where H_0 is the free continuum model Hamiltonian (see SM Sec. 6). The Hartree term and Fock terms take the form

$$\Sigma_H = \sum_{\alpha,\beta,q,k,k'} \frac{V(\mathbf{q})}{A_{tot}} \langle c_{\alpha,k+q}^\dagger c_{\alpha,k} \rangle c_{\beta,k'-q}^\dagger c_{\beta,k'} ,$$

$$\Sigma_F = - \left[\sum_{\alpha,\beta,q,k,k'} \frac{V(\mathbf{q})}{A_{tot}} \langle c_{\alpha,k+q}^\dagger c_{\beta,k'} \rangle c_{\beta,k'-q}^\dagger c_{\alpha,k} + h.c. \right] ,$$

where $\langle \mathcal{O} \rangle$ stands for the expectation value of operator \mathcal{O} from all the occupied electrons for a given electron filling n . We assume there is neither spontaneous translational symmetry breaking nor spontaneous polarization of spins and valleys. In general, translational symmetry breaking will enlarge the unit cell, and spin/valley polarization will break the 4-fold spin-valley degeneracy, both of which may lead to insulating states at non-integer fillings n/n_s . Such non-integer filling insulating states are not observed in our experiment (see main text Fig. 1), so we assume translation symmetry and spin-valley degeneracy are unbroken. Thus $\langle c_{\alpha,k}^\dagger c_{\beta,k'} \rangle$ is nonzero only if $\mathbf{k} - \mathbf{k}' = m_1 \mathbf{g}_1 + m_2 \mathbf{g}_2$ ($m_1, m_2 \in \mathbb{Z}$) and α, β belong to the same spin and valley, where \mathbf{g}_1 and \mathbf{g}_2 are the reciprocal vectors of the moiré superlattice.

To perform the self-consistent calculation, we take a moiré momentum lattice cut off of the single-particle Hamiltonian H_0 so that it contains 146 bands (i.e., is a 146×146 matrix) per spin per valley. In the first step, we add to H_0 a small Hermitian random matrix H_{seed} as a seed for all possible spontaneous symmetry breakings, and diagonalize $H_0 + H_{seed}$, after which we calculate the expectation values in Σ_H and Σ_F at the desired fixed filling. Then we iteratively diagonalize the full Hamiltonian $H = H_0 + \Sigma_H + \Sigma_F$ (the initial seed is no longer added after the first step) and calculate Σ_H and Σ_F at the fixed filling until convergence (until the total Hartree-Fock energy $E_{HF} = \langle H_0 + \frac{1}{2}(\Sigma_H + \Sigma_F) \rangle$ changes less than 0.01meV in one step). In the calculation of Fig. 1C and Fig. S10, we take $\frac{|\mathbf{g}_1|V(\mathbf{g}_1)}{\sqrt{3}} = 10\text{meV}$, relaxation parameter $u_0 = 0.3$ (see SM Sec. 6), and add the random initial seed H_{seed} to allow for spontaneous symmetry breakings.

Our Hartree-Fock calculations for integer fillings $n = Nn_s$ with an initial Hermitian random matrix symmetry breaking seed H_{seed} show that the C_{3z} symmetry is spontaneously broken, but $C_{2z}\mathbb{T}$ is preserved. The Hartree-Fock band structures and the density of states for $N = 0,1,2,3,4$ are shown in Fig. S10A and Fig. S11, respectively. For fillings $n/n_s = 0,1,3,4$, we find the band structures are semimetallic with 2 Dirac points at the Fermi energy. For filling $n/n_s = 2$, the band structure has a small indirect gap at the Fermi energy. Lastly, we comment that the realistic tBLG samples may also have external C_{3z} breakings due to uniaxial strains, as revealed by scanning tunneling microscope experiments of tBLG (5-8).

6. Hofstadter Butterfly Calculation

We calculate the Hofstadter butterfly of the tBLG continuum model, which can be written in real space as

$$H_0 = \int d^2\mathbf{r} \sum_{\eta,s} c_{\eta,s}^\dagger(\mathbf{r}) \begin{pmatrix} \hbar v \boldsymbol{\sigma}^\eta \cdot (-i\nabla) & T^\eta(\mathbf{r}) \\ T^{\eta\dagger}(\mathbf{r}) & \hbar v \boldsymbol{\sigma}^\eta \cdot (-i\nabla) \end{pmatrix} c_{\eta,s}(\mathbf{r}) ,$$

where $c_{\eta,s}(\mathbf{r}) = (c_{A,t,\eta,s}(\mathbf{r}), c_{B,t,\eta,s}(\mathbf{r}), c_{A,b,\eta,s}(\mathbf{r}), c_{B,b,\eta,s}(\mathbf{r}))^T$ is the free electron basis ($c_{a,l,\eta,s}(\mathbf{r})$ for an electron in sublattice a , layer $l = t, b$ (for top and bottom), valley η ($= \pm 1$ for K, K') and spin s), $\boldsymbol{\sigma}^\eta = (\eta\sigma_x, \sigma_y)$ are the Pauli matrices, $T^\eta(\mathbf{r}) = \sum_j^3 T_j^\eta e^{i\eta q_j \mathbf{r}}$, and the 3 matrices T_j are given by

$$T_j^\eta = w \begin{pmatrix} u_0 & e^{i2\pi\eta(j-1)/3} \\ e^{-i2\pi\eta(j-1)/3} & u_0 \end{pmatrix} .$$

The dimensionless parameter u_0 characterizes the lattice relaxation. It equals to 1 when there is no relaxation. For 0.45° , we estimate the relaxation parameter to be $u_0 = 0.3$ (9, 10), which we use in all of our calculations. Because of the presence of C_{2z} symmetry and the absence of spin-orbital coupling, the Hofstadter butterflies of all the 2 spins and 2 valleys are identical (excluding the Zeeman energy). The Zeeman energy is negligibly small ($0 < E_z < 1.85 \text{ meV}$ for the magnetic field

range in the experiment, assuming the $g = 2$) compared to the band energies, which is thus ignored in our Hofstadter butterfly calculations.

In real samples, interlayer uniaxial strain may exist which breaks the C_{3z} symmetry of tBLG (more information shown in SM Sec. 7). In addition, electron-electron interactions may also spontaneously break the C_{3z} symmetry, as our Hartree-Fock calculations show (SM Sec. 5). We find the Hofstadter butterfly with a C_{3z} symmetry breaking agrees better with the experimental data. In particular, adding C_{3z} symmetry breaking allows us to reproduce the reemergence of the $(0,0)$, $(0, \pm 1)$ and $(0, \pm 2)$ gaps at high B_{\perp} field ($\phi > \phi_0$), one of the experimental details.

The strain induced breaking of C_{3z} symmetry is shown in SM Sec. 7, where due to strain the moiré Brillouin zone vectors \mathbf{q}_j for $j = 1, 2, 3$ are no longer related to each other via three-fold rotation. The resultant moiré Brillouin zone is an irregular hexagon. Alternatively, the effect of the C_{3z} symmetry breaking can also be incorporated in the interlayer hopping matrix by changing T_1^{η} into γT_1^{η} (γ is a dimensionless parameter) while keeping T_2^{η} and T_3^{η} . In our Hofstadter butterfly calculations, we use the first approach to properly take strain into account (SM Sec. 7). We have verified that the qualitative features of Hofstadter butterfly are the same in both approaches.

Furthermore, to partially include the effect of Coulomb interactions between electrons, we add the following term to the Hamiltonian H_0 as an approximate Hartree term:

$$H_I = U_0 \int d^2\mathbf{r} \sum_{\eta,s} \left(\sum_{j=1}^6 e^{i\mathbf{g}_j \cdot \mathbf{r}} \right) c_{\eta,s}^{\dagger}(\mathbf{r}) c_{\eta,s}(\mathbf{r}),$$

where \mathbf{g}_j are the six smallest reciprocal vectors of the moiré superlattice. Our Hartree-Fock numerical calculations at zero magnetic field show this is the leading term in the Hartree potential. The coefficient U_0 depends on the electron filling fraction. For electron (hole) doping, $U_0 > 0$ ($U_0 < 0$).

The Hamiltonian is diagonalized in the Landau level basis of monolayer graphene $|l, N, Y\rangle$, where N is the Landau level index, Y is the guiding center, and we have chosen the Landau gauge. In the Landau level basis, the matrix elements of the interlayer tunneling Hamiltonian $T^{\eta}(\mathbf{r})$ involves the evaluation of the following matrix element:

$$\langle t, N, Y | e^{i\mathbf{q}_j \cdot \mathbf{r}} | b, M, Y' \rangle = \delta_{Y, Y' + \mathbf{q}_j \cdot \ell^2} e^{\frac{i\mathbf{q}_j \cdot (Y + Y')}{2}} \chi_{N,M}(\mathbf{q}),$$

$$\chi_{N,M}(\mathbf{q}_j) = \begin{cases} e^{-\left(\frac{q_j \ell}{2}\right)^2} \frac{\sqrt{M!}}{\sqrt{N!}} \left(\frac{(-q_{jx} + iq_{jy})\ell}{\sqrt{2}} \right)^{N-M} L_M^{N-M} \left(\frac{q_j^2 \ell^2}{2} \right) & N \geq M \\ e^{-\left(\frac{q_j \ell}{2}\right)^2} \frac{\sqrt{N!}}{\sqrt{M!}} \left(\frac{(q_{jx} + iq_{jy})\ell}{\sqrt{2}} \right)^{M-N} L_N^{M-N} \left(\frac{q_j^2 \ell^2}{2} \right) & M > N. \end{cases}$$

Here L_M^N are the associated Laguerre polynomials. Hence the interlayer tunneling in the Landau level basis couples a guiding center Y from one layer to another guiding center $Y' = Y \pm \Delta_j$, where $\Delta_j = q_{jx} \ell^2$ from the other layer. Here ℓ is the magnetic length. For the C_{3z} symmetric unstrained case, as well as for the C_{3z} broken strained case under our choice of strain parameters (which constraints $q_{2x} = -q_{3x}$) (SM Sec. 7 and Fig. S13B), the interlayer term can be interpreted as a 1D lattice of guiding centers with nearest neighbor hopping and the lattice constant $\Delta = |q_{2x}| \ell^2$.

Similarly, the Hartree term H_I , couples the guiding center Y with the guiding centers $Y'' = Y \pm \delta_j$, where $\delta_j = g_{jx} \ell^2$ within the same layer. The values taken by g_{jx} are $0, \pm \Delta / \ell^2, \pm 2\Delta / \ell^2$. In this guiding center chain picture, the Hartree term only further introduces next nearest neighbor hopping.

The guiding center chain becomes periodic for the rational flux ratio through the moiré unit cell, i.e. when

$$A_m \ell^2 = 2\pi \frac{p}{q}, \quad A_m = 3\sqrt{3}|K|^2(\theta^2 - \nu^2 \epsilon) \ell^2,$$

For positive integers p and q . Here $|K| = 4\pi/3a_0$, and ϵ, ν are the strain and Poisson ratio [see SM Sec. 7]. The above relation for the area of the strained moiré Brillouin zone is only valid for the specific strain we have chosen for the purpose of numerical efficiency in Hofstadter butterfly calculation. In the limit of no strain one flux through moiré unit cell corresponds to $B \sim 25 \theta^2$ magnetic field in Tesla. In the guiding center chain picture, the number of orbitals on each guiding center site is set by the number of Landau levels kept within a cut-off to obtain convergent result for the Hofstadter spectrum. Overall the dimension of the matrix to be diagonalized is $(4N_c + 2)q$, where the monolayer graphene Landau levels ranging from $-N_c$ to N_c are kept within the cutoff. The value of N_c is set by ~ 500 meV energy window on either side of Dirac point, with some variation for smoothing. Rest of the diagonalization procedure follows Bistritzer et. al (11).

The gaps in the Hofstadter spectrum have associated topological indices (σ, s) , where σ refers to the Hall conductivity and s is associated with moiré band filling. To calculate these indices, we first notice the gaps in the Hofstadter spectrum and calculate the Landau level filling ν_{LL} at those gaps. Next the Landau level fillings are plotted as function of flux ratio. The gap trajectories plotted this way follow simple relation:

$$\nu_{LL} = \sigma + s \frac{p}{q},$$

and the integers σ and s are simply the intercept and the slope of these gap trajectories.

In Fig. S12B-C, we compare the Hofstadter butterflies for $U_0 = 0$ (corresponding to no doping), both of which have a 0.4% strain breaking the C_{3z} symmetry (see SM Sec. 7), and $U_0 = 10$ meV (corresponding to electron doping), where one can see the $(4, s)$ gaps (with 4-fold degeneracy from spin and valley) are suppressed by U_0 . This suggest that the absence of $(4, s)$ gaps for $s \geq 2$ (where the sample is electron doped) in the experiment may be due to interaction effects.

7. Uniaxial strain and C_{3z} symmetry

In general, both graphene layers are likely to experience strain that may be unavoidable during fabrication process. The signature of strain is observed in the spectroscopy data at the magic angle, where the C_{3z} rotational symmetry broken moiré pattern is observed (5-8). Here we outline the procedure to take strain effects into account in our theoretical calculations.

Let the vectors \mathbf{K}_i , (for $i = 1, 2, 3$) denote the momentum space position of the three K valley points of a monolayer of graphene, such that:

$$\mathbf{K}_1 = \begin{pmatrix} |\mathbf{K}| \\ 0 \end{pmatrix}, \mathbf{K}_2 = \begin{pmatrix} -\frac{|\mathbf{K}|}{2} \\ \frac{\sqrt{3}}{2} |\mathbf{K}| \end{pmatrix}, \mathbf{K}_3 = \begin{pmatrix} -\frac{|\mathbf{K}|}{2} \\ -\frac{\sqrt{3}}{2} |\mathbf{K}| \end{pmatrix}, \quad |\mathbf{K}| = \frac{4\pi}{\sqrt{3}a_0}.$$

Rotation of a graphene layer by an angle θ is generated by the rotation matrix

$$R(\theta) = \begin{pmatrix} \cos \theta & -\sin \theta \\ \sin \theta & \cos \theta \end{pmatrix},$$

while application of uniaxial strain ϵ in a graphene layer along a strain direction at angle φ from x -axis is generated by the strain tensor

$$S(\epsilon, \varphi) = R(\varphi)^{-1} \begin{pmatrix} 1 - \epsilon & 0 \\ 0 & 1 + \nu \epsilon \end{pmatrix} R(\varphi),$$

where $\nu = 0.12$ is the Poisson ratio of graphene and the sign of ϵ dictates compression or stretch.

We consider the tBLG under strain as a two-step process, first, the top and the bottom graphene layers are rotated by angles $-\frac{\theta}{2}$ and $\frac{\theta}{2}$ respectively as shown in the Fig. S13A, then independent uniaxial strain $S(\epsilon_t, \varphi_t)$ and $S(\epsilon_b, \varphi_b)$ are applied to the two layers as shown in the Fig. S13B. The

hexagonal moiré Brillouin zone is constructed by taking the difference between the new positions of the three K valley Dirac points of the two layers.

$$\mathbf{q}_i = \mathbf{K}_i^t - \mathbf{K}_i^b = \left[S(\epsilon_t, \varphi_t)R\left(-\frac{\theta}{2}\right) - S(\epsilon_b, \varphi_b)R\left(\frac{\theta}{2}\right) \right] \mathbf{K}_i.$$

In the limit of zero strain, the three high symmetry moiré vectors

$$\mathbf{q}_1 = \begin{pmatrix} 0 \\ -2K \sin \frac{\theta}{2} \end{pmatrix}, \mathbf{q}_2 = \begin{pmatrix} \sqrt{3}K \sin \frac{\theta}{2} \\ K \sin \frac{\theta}{2} \end{pmatrix}, \mathbf{q}_3 = \begin{pmatrix} -\sqrt{3}K \sin \frac{\theta}{2} \\ K \sin \frac{\theta}{2} \end{pmatrix},$$

shown in right of Fig. S13A are related by C_{3z} rotational symmetry. The resultant moiré Brillouin zone is a regular hexagon.

Generally under strain the C_{3z} symmetry is broken and the moiré Brillouin zone is an irregular hexagon as shown in the Fig. S13B. For the numerical efficiency in the Hofstadter butterfly calculations, we consider the form of strain that deforms the hexagonal moiré Brillouin zone in a specific form shown in the Fig. S13C, which still breaks the C_{3z} symmetry. For this specific kind of strain deformation, the strain in the top and bottom layer is generated by $S(\epsilon, \varphi)$ and $S(-\epsilon, \varphi)$ respectively. The strain angle φ is determined under the following constraints on the moiré Brillouin zone vectors \mathbf{q}_i :

$$\begin{aligned} q_{1x} &= 0, \quad q_{2x} = -q_{3x}, \\ q_{2y} &= q_{3y} = -\frac{q_{1y}}{2}. \end{aligned}$$

We note that this way of breaking C_{3z} makes \mathbf{q}_1 different from \mathbf{q}_2 and \mathbf{q}_3 . The effect of such a deformation on the Hofstadter butterfly is similar to the effect of changing T_1^η into γT_1^η (γ is a dimensionless parameter) while keeping T_2^η and T_3^η , as we have checked numerically. Heuristically, this is because enlarging \mathbf{q}_1 increases the on-site (momentum site) energy (the Dirac fermion term) difference between \mathbf{k} and $\mathbf{k} + \mathbf{q}_1$, which hop with each other by matrix T_1^η ; perturbatively, this is similar to reducing the magnitude of T_1^η while maintaining the Dirac kinetic energy difference (which is proportional to q_1). At zero magnetic field, both ways of breaking C_{3z} shift the Dirac points away from K_M and K_M' points in a similar way.

8. Landau fan in the large magnetic field limit

In the large magnetic field limit, both the experiment and the numerical calculation demonstrate that the Landau fan is dominated by $(4, s)$, $(8, s)$, \dots , where s is an integer. Here we give a heuristic understanding of these gaps from the zero twist-angle limit. We note that at zero twist angle (assuming AB stacking), there are only two low energy graphene bands which are connected by a quadratic Dirac point of helicity $\eta = \pm 2$ at each graphene valley (\pm signs for original graphene valleys K and K' , respectively). So if we view the two graphene valleys as decoupled, the Dirac helicity of each AB-stacked graphene valley matches the fragile topology of the tBLG.

The quadratic Dirac point band touching at valley η ($\eta = \pm 1$ for K and K') of the zero-twist-angle bilayer graphene can be effectively described by a $k \cdot p$ Hamiltonian $h_{BLG}^\eta(k) = \eta(k_x^2 - k_y^2)\sigma_x + 2k_x k_y \sigma_y$. In a magnetic field, LLs are developed at the quadratic touching bands at each spin and valley, leading to in total 8 degenerate zero mode LLs, and 4-fold degenerate non-zero-mode LLs with energies linear in B . As a result, the system with 4-fold spin-valley degeneracy has LL gaps denoted by $(4t, 0)$ with $t = \pm 1, \pm 2, \dots$, where (C, s) denotes a gap with Chern number C and electron filling s at zero magnetic field ($s = 0$ for CNP). Fig. S14A illustrates such LLs and the LL gaps between them, where gap A has Chern number $C = 4$, and gap G has a Chern number $C = 8$ (counting the 4-fold spin-valley degeneracy). We note that this LL picture is valid because we are considering magnetic fields corresponding to negligibly small magnetic fluxes per original graphene unit cell; hence, we are not considering the Hofstadter butterfly of the bands of untwisted bilayer graphene in the original graphene Brillouin zone. The spectra are therefore well characterized by the LLs of the $k \cdot p$ quadratic Dirac Hamiltonian $h_{BLG}^\eta(k)$ at two graphene valleys, and no Hofstadter physics in the original graphene BZ is expected.

In twisted bilayer graphene, at sufficiently large magnetic field, the Hofstadter spectrum can be thought of as adiabatically deformed from the LLs in the untwisted limit (see Fig. S14A-B), during which the original LL gaps in the untwisted limit remain open above a certain threshold magnetic field. With the two layers twisted relative to each other, a spatially periodic moiré superlattice potential arises, and defines a moiré unit cell (at zero magnetic field) of area Ω_m . Consider some large magnetic flux per moiré unit cell $\phi = p\phi_0$, where p is an integer (so the moiré superlattice translation symmetry is unbroken). Before we turn on the moiré potential, by Streda formula, the number of electron states each LL can accommodate per moiré unit cell is p . Therefore, when the moiré potential is turned on, each LL (per spin per valley) in the untwisted limit will split into p subbands. Each subband j ($1 \leq j \leq p$) has $n_j = 1$ electron state per area Ω_m and may carry some Chern number σ_j ($\sum_{j=1}^p \sigma_j = 1$). Fig. S14B gives some illustrative examples of the splitting of the first LL (at one spin one valley) into p subbands at integer fluxes $p = 2,3,4,5$, and the Chern numbers σ_j of the subbands at each flux $p\phi_0$ are denoted by the red numbers. We note that here we only require p to be large enough so that the original LL gaps (e.g., gaps A and G in Fig. S14B) are large enough (larger than the typical zero-magnetic-field moiré band widths) and remain open as the moiré potential is turned on. In our case of twist angles around 0.5° , this requires p greater than 2 or 3.

When the magnetic flux changes, by Streda formula, the number of electron states n_j per area Ω_m of a subband j at flux $p\phi_0$ satisfies $dn_j/d\phi = \sigma_j/\phi_0$. Therefore, if $\sigma_j \neq 0$, a subband j at flux $p\phi_0$ cannot uniquely deform into a subband $1 \leq j' \leq p+1$ at flux $(p+1)\phi_0$, since $n_j = n_{j'} = 1$. If a subband at flux $p\phi_0$ carry a negative Chern number $\sigma_j < 0$, its electron density will decrease to zero before or at flux $(p+1)\phi_0$, so it has to merge with another subband. An example is the Chern number -1 subband at flux $2\phi_0$ in Fig. S14B, which merges with another subband at flux $3\phi_0$. If a subband at flux $p\phi_0$ has a Chern number $\sigma_j > 0$, it has to split into $\sigma_j + 1$ subbands ($\sigma_j > 0$) as flux increases by 1 (for example, The Chern number 2 subband at flux $2\phi_0$ and the Chern number 1 subbands at fluxes $3,4,5\phi_0$ in Fig. S14B). Therefore, a subband j can adiabatically sustain itself as a single isolated subband for a wide range of magnetic fluxes only if its Chern number $\sigma_j = 0$ (e.g., the Chern number 0 subbands in Fig. S14B). Non-zero chern number bands have to split at some point as a function of the magnetic field.

These subbands carrying Chern number $\sigma_j = 0$, which remain a single isolated subband for a wide range of magnetic field, then give rise to the series of gaps $(4, s)$, $(8, s)$..., where (C, s) denotes a gap with Chern number C and electron filling $s = n(\phi = 0)/n_s$ at zero magnetic field, and $n_s = 4/\Omega_m$ with 4-fold spin-valley degeneracy considered. The reasoning is as follows:

First, given that the original LL gaps (in the untwisted limit) remain open in a wide range of sufficiently large magnetic field (large magnetic fluxes per moiré unit cell, but still much smaller than one magnetic flux per microscopic graphene unit cell), they correspond to $(4t, 0)$ gaps in the tBLG (counting the 4-fold spin-valley degeneracy). For example, gaps A and G in Fig. S14B correspond to the $(4,0)$ gap (occupying all the zero-mode LLs and below) and $(8,0)$ gap (occupying the zeroth and first LLs), respectively.

Then, in the illustrative Fig. S14B, the gaps C, D, E, F are separated with gap A by 1 to 4 Chern number 0 subbands, respectively. Accordingly, they correspond to a series of Chern number 4 gaps $(4,1)$, $(4,2)$, $(4,3)$, $(4,4)$, respectively. In particular, they can remain open over a wide range of magnetic fluxes, since the Chern number 0 subbands separating them can remain isolated without restriction from the Streda formula. In contrast, gap B (with quantum numbers $(0,3)$), which differs from gap A by a Chern number -1 band at flux $2\phi_0$, has to close readily at flux $3\phi_0$. This shows that the splitting of the first LL by moiré potential would most likely give rise to the $(4, s)$ series of gaps extending over a wide range of fluxes (and similarly $(8, s)$ for the second LL, and higher). For the zero-th LLs, similarly they could develop a Hofstadter spectrum with certain $(0, s)$ gaps remaining open in a wide range of magnetic fluxes at large enough magnetic field.

Experimental data (main text Fig. 2) and numerical calculation (Fig. S12) show that this can happen, e.g., the (0,0) and ($\pm 1,0$) gaps (after they are interrupted by the ($\pm 4,0$) gaps).

9. Tight-binding model for Fig. 3A-B

The Hofstadter butterfly in main text Fig. 3A-B are calculated with the following 2-band tight-binding model on a 2D square lattice (of lattice constant 1):

$$H_{\text{TB}}(\mathbf{k}) = (M - \cos k_x - \cos k_y)\sigma_z + A(\sigma_x \sin k_x + \sigma_y \sin k_y),$$

where M and $A > 0$ are constants, $\sigma_{x,y,z}$ are Pauli matrices in the band basis, and $\mathbf{k} = (k_x, k_y)$ is the quasimomentum in the BZ. We note that this model can be viewed as half of the Bernevig-Hughes-Zhang model (13).

The valence band and conduction band of this model both have Chern numbers 0 if $|M| > 2$. In contrast, when $|M| < 2$, the valence band and conduction band have Chern numbers $\pm M/|M|$, respectively. Fig. 3A is calculated by setting $M = 3$ and $A = 2$, for which both bands are trivial bands with Chern number 0. Fig. 3B is calculated by setting $M = 1$ and $A = 2$, for which the valence and conduction bands carry Chern number ± 1 , respectively.

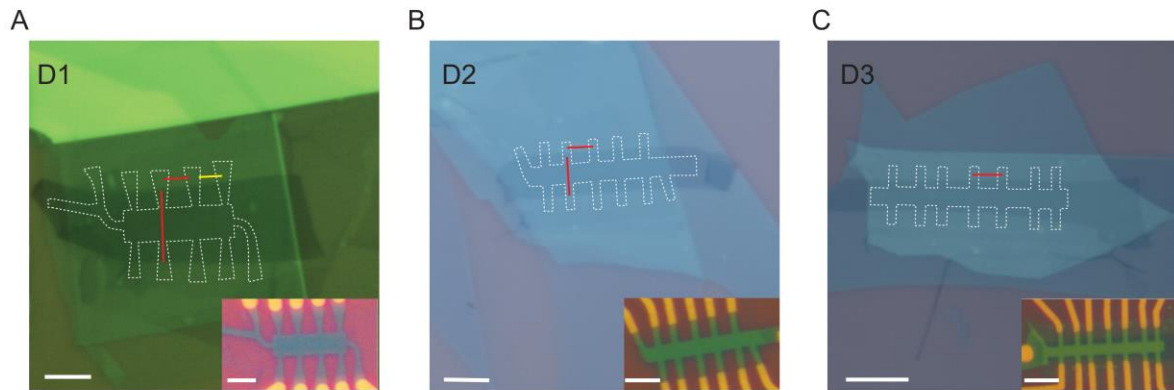


Fig. S1. Optical microscope images of stacks and devices. Red lines in (A) mark the contact pairs which are further labeled as device D1-1 (0.45°). The contact pair indicated by yellow line is labeled as D1-2 (0.44°) with measured data shown in Fig. S8B. Device D2 (0.38°) and device D3 (0.34°) are measured with contact pairs indicated by red lines in (B) and (C), with corresponding results displayed in Fig. S7 and S8. The outlines of fabricated Hall bars are demonstrated with the white dashed lines. All scale bars are $5\ \mu\text{m}$.

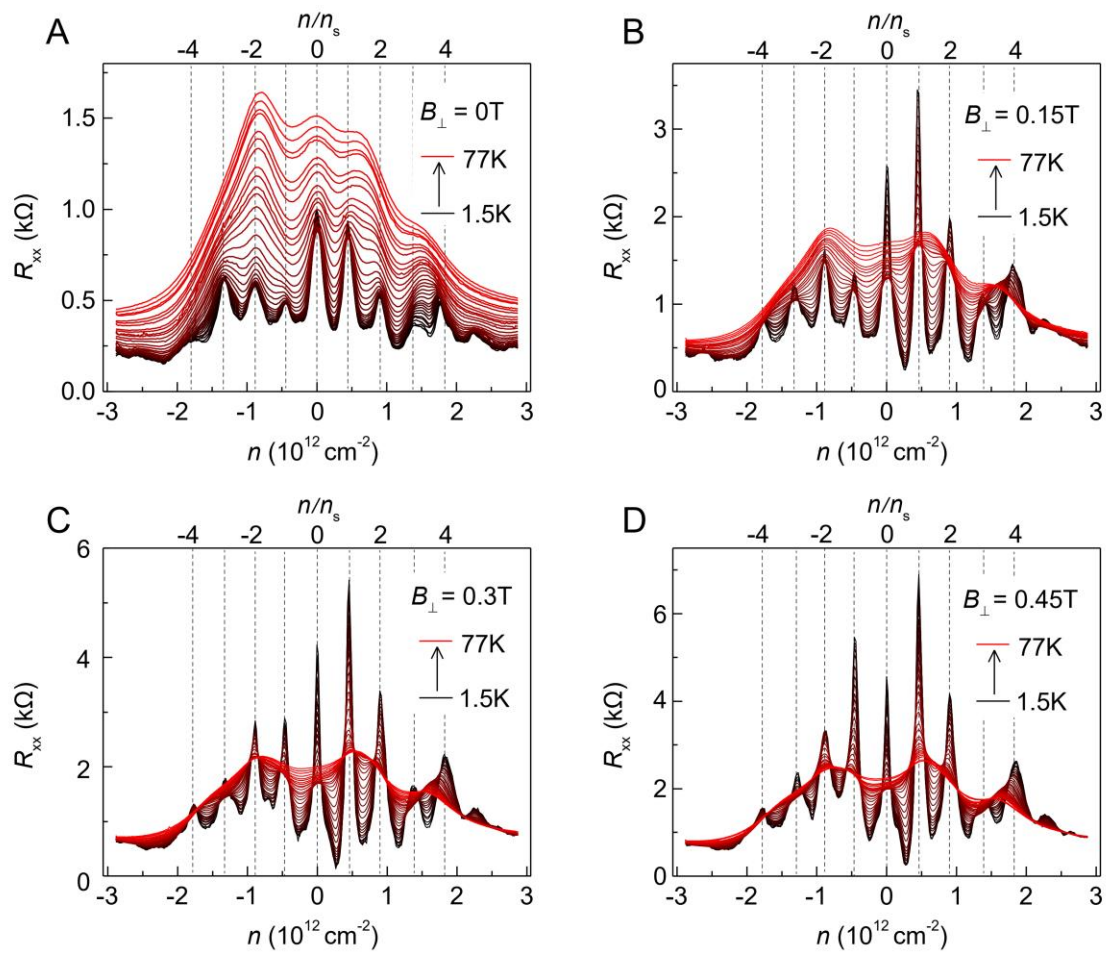


Fig. S2. Magnetic field induced metal-insulator transition. Longitudinal resistance R_{xx} vs. carrier density n at various temperatures measured at a magnetic field B_{\perp} of 0T (A), 0.15T (B), 0.3T (C) and 0.45T (D). Data is measured from D1-1 (0.45°).

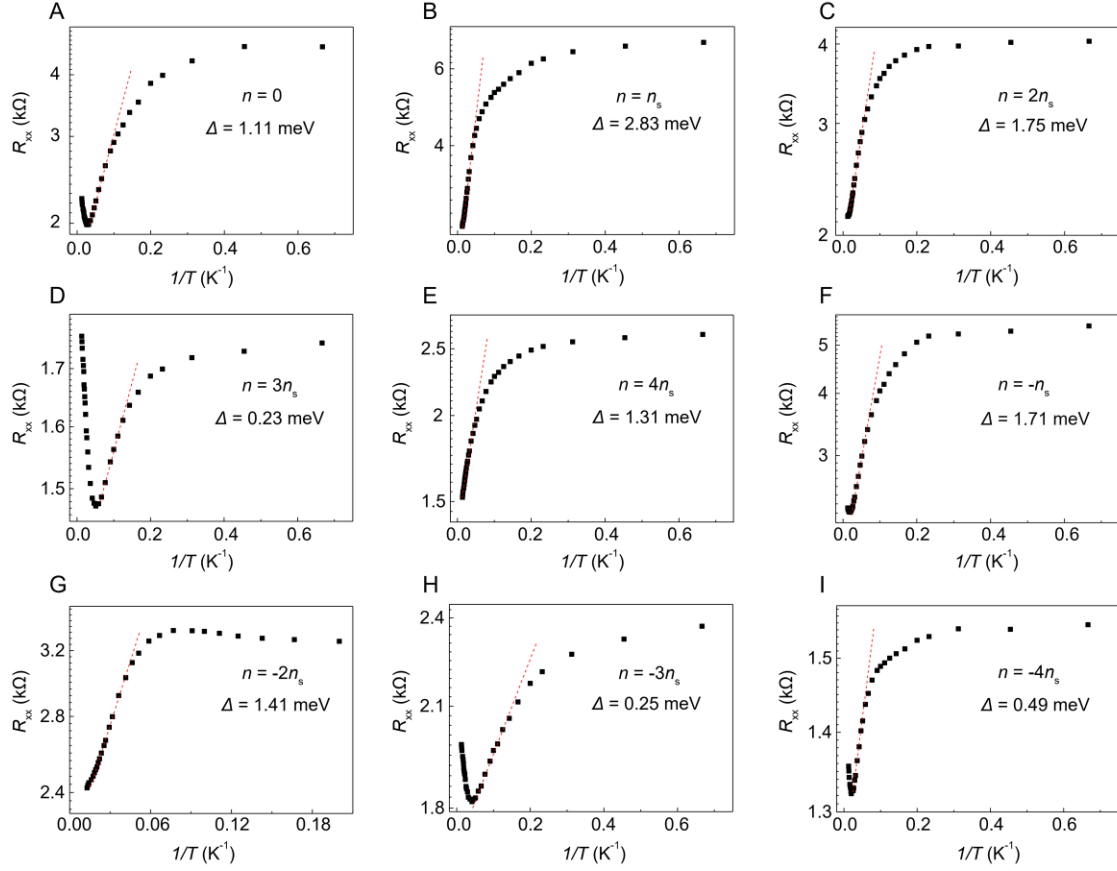


Fig. S3. Extraction of gaps in all integer filling states. (A-I) Longitudinal resistance R_{xx} vs. inverse temperature $1/T$ at various integer fillings $n=Nn_s$ and $B_{\perp} = 0.45T$. The straight dashed lines are fits to $R_{xx} \sim \exp(\Delta/2kT)$ temperature activated behavior. Data is measured from D1-1 (0.45°).

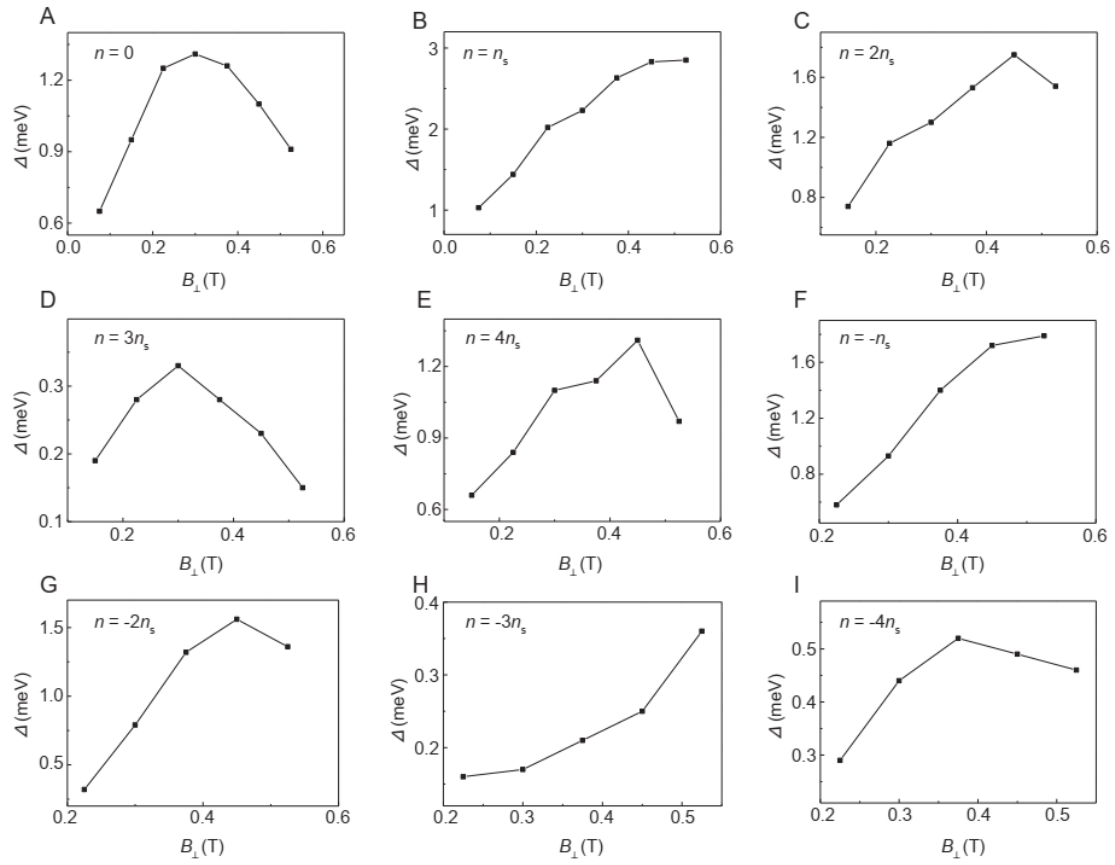


Fig. S4. Gap evolution with B_{\perp} at all integer filling stages. (A-I) Magnetic field B_{\perp} dependent gaps at various integer fillings $n=Nn_s$ extracted from $R_{xx} \sim \exp(\Delta/2kT)$ temperature activated behavior. Data is measured from D1-1 (0.45°).

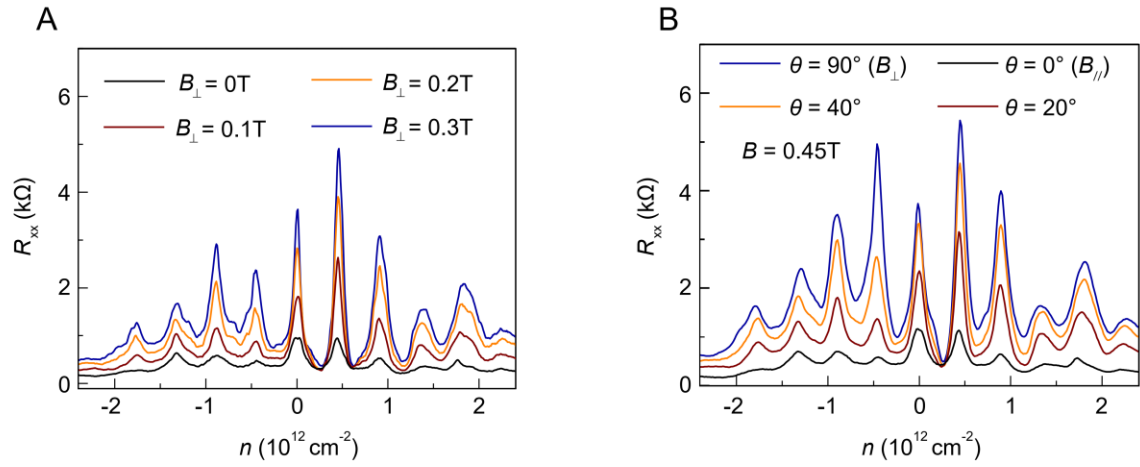


Fig. S5. R_{xx} vs. carrier density n at various magnetic field. (A) R_{xx} vs. n at different perpendicular magnetic field B_{\perp} . (B) R_{xx} vs. n at fixed total field $B = 0.45\text{T}$ with different tilt angles. Data is measured from D1-1 (0.45°) at a temperature of 1.5K

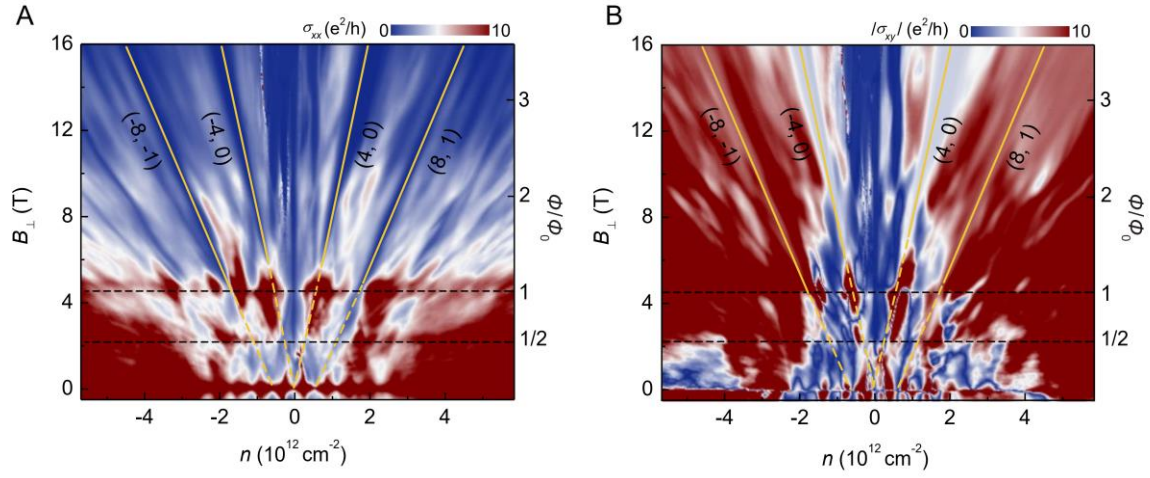


Fig. S6. Hofstadter butterfly measured from D1-1. Color plot of longitudinal conductivity $\sigma_{xx} = \rho_{xx}/(\rho_{xx}^2 + R_{xy}^2)$ (A) and magnitude of hall conductivity $|\sigma_{xy}| = |R_{xy}|/(\rho_{xx}^2 + R_{xy}^2)$ (B) as a function of carrier density n and B_{\perp} measured at a temperature of 1.5K. Yellow solid lines indicate gaps with different Chern numbers and yellow dashed lines give sight guidance for tracing to different moiré bands. Black dashed lines mark the positions of magnetic flux values ($\phi_0/2$ and ϕ_0) through the moiré unit cell.

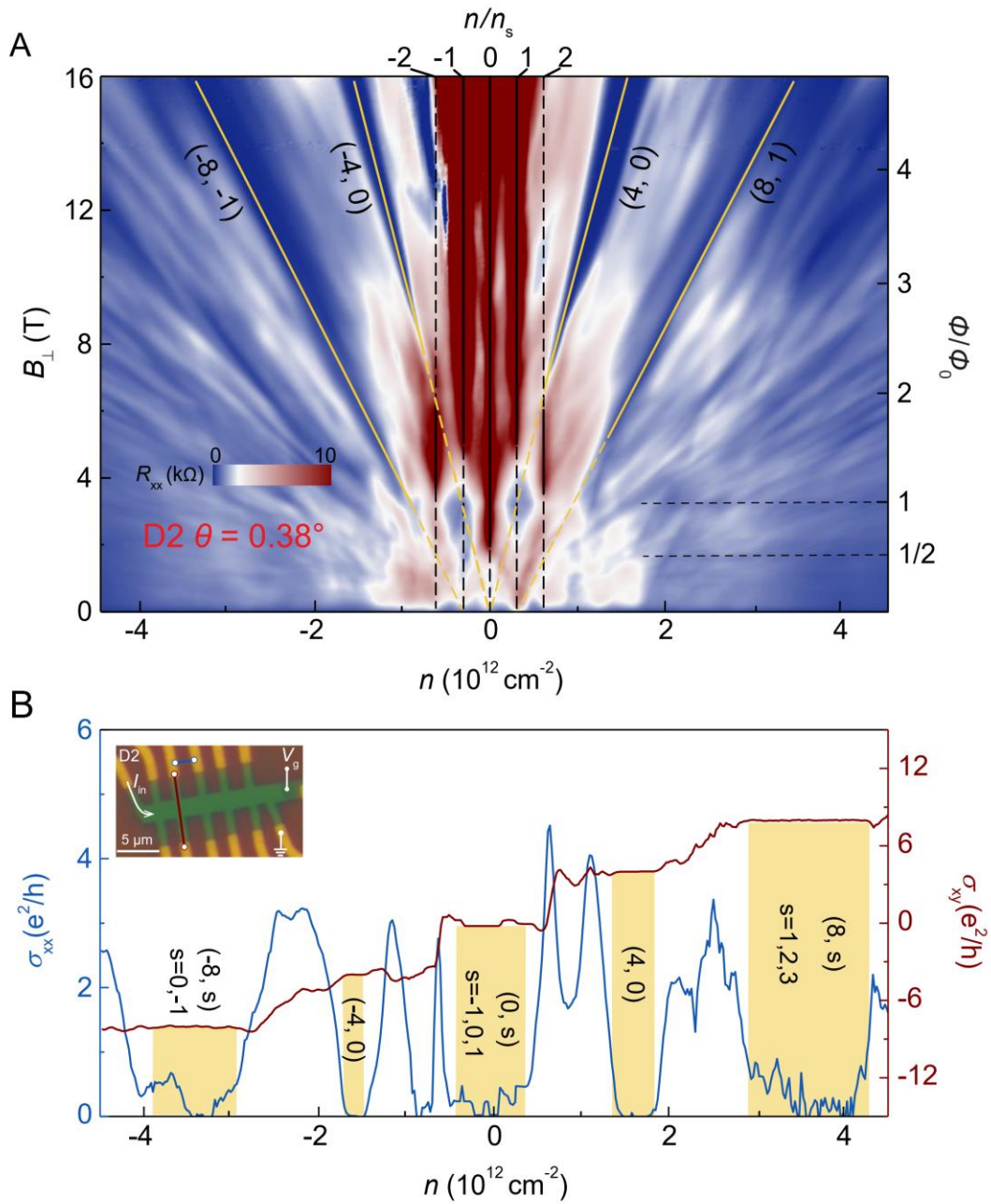


Fig. S7. Hofstadter butterfly spectrum in 0.38° tBLG (D2). (A) Color plot of longitudinal resistance R_{xx} as a function of carrier density n and B_{\perp} . Black and yellow solid lines indicate gaps with different Chern numbers and extended dashed lines give sight guidance for tracing to different moiré bands. The horizontal dashed lines mark the positions of magnetic flux values ($\phi_0/2$ and ϕ_0) through the moiré unit cell. (B) Longitudinal conductivity σ_{xx} and hall conductivity σ_{xy} vs. carrier density n measured at a maximum magnetic field of 16T. Both (A) and (B) are measured at a temperature of 1.5K.

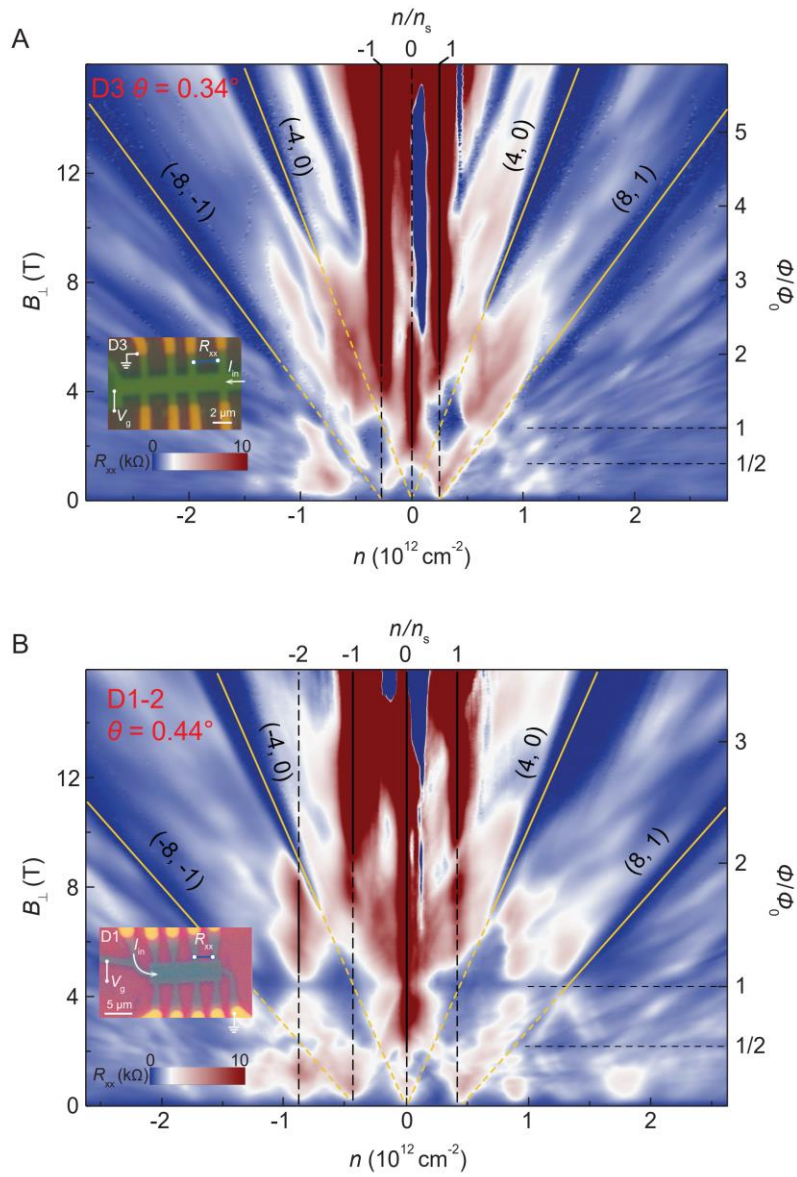


Fig. S8. **Hofstadter butterfly spectrums measured from device D3 (0.34°) and D1-2 (0.44°).** Color plot of longitudinal resistance R_{xx} as a function of carrier density n and B_{\perp} measured from device D3 (A) and device D1-2 (B). Inserts show optical images and measurement configurations of devices D3 and D1-2. Black and yellow solid lines indicate gaps with different Chern numbers and extended dashed lines give sight guidance for tracing to different moiré bands. The horizontal dashed lines mark the positions of magnetic flux values ($\phi_0/2$ and ϕ_0) through the moiré unit cell. Both (A) and (B) are measured at a temperature of 1.5K.

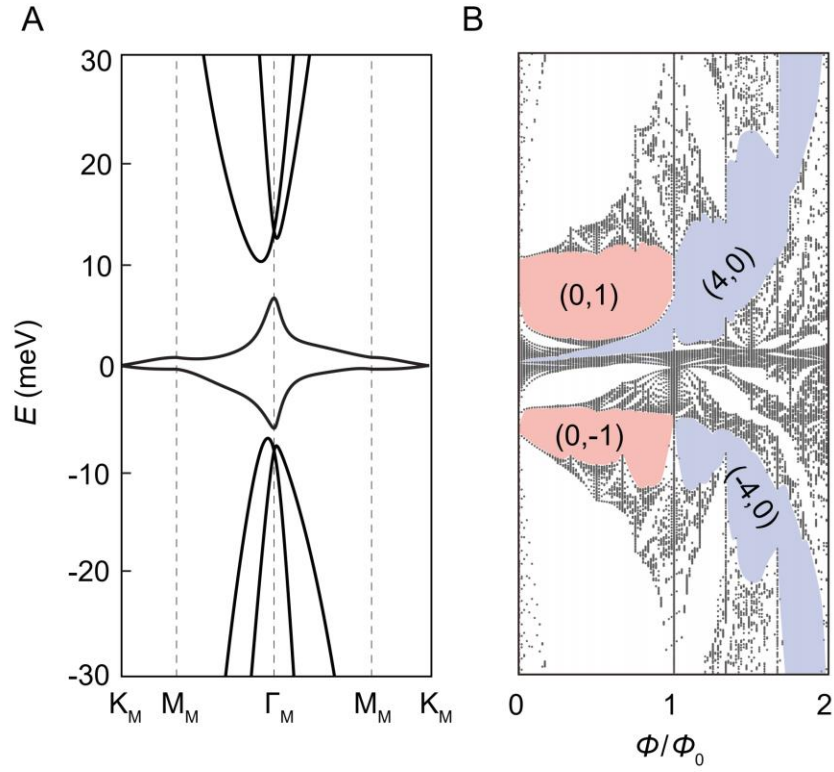


Fig. S9. **(A)** The band structure of the ten-band tight-binding model (one spin one valley) in Ref (12) at zero magnetic field. **(B)** The Hofstadter butterfly of the ten-band tight-binding model, where (C, s) labels a Hofstadter gap with Chern number C (counting the 4-fold spin-valley degeneracy) and zero-magnetic-field filling $s = n/n_s$ per unit cell. Both figures are replotted from Ref (2).

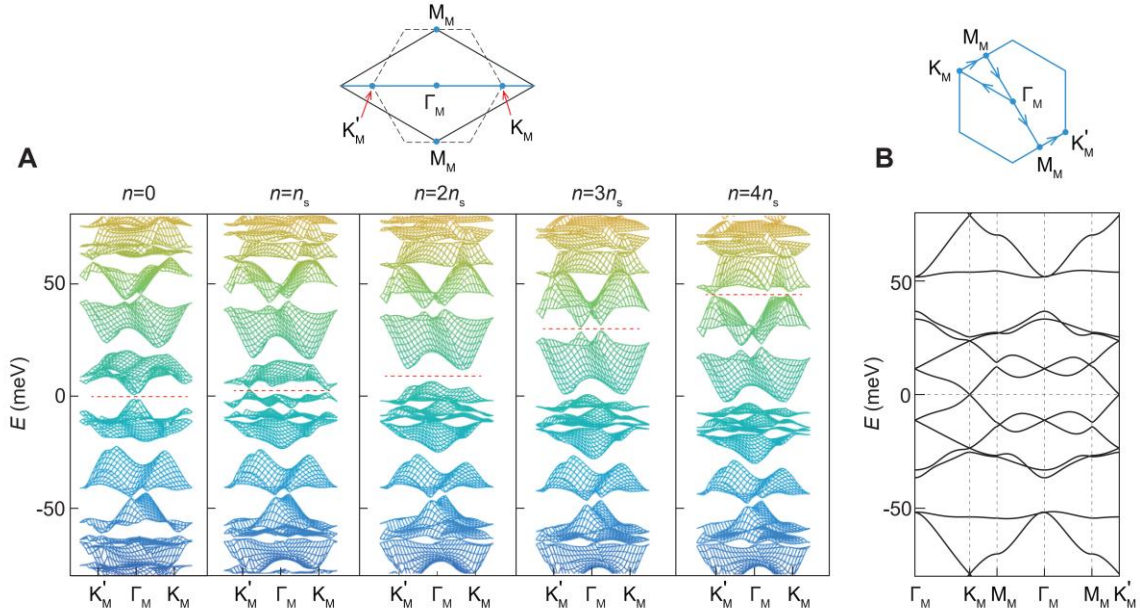


Fig. S10. Band structures simulation. (A) The band structure of the 0.45° tBLG under the Hartree-Fock approximation considering Coulomb interaction $\frac{|g_1|V(g_1)}{\sqrt{3}} = 10\text{meV}$ between electrons (g_1 : moiré reciprocal vector) at various integer fillings $n=Nn_s$, where the Fermi energies are indicated with red dashed lines. The 2D band structures are plotted in the diamond (instead of honeycomb) moiré Brillouin zone (see the top insert in (A)), and viewed from the side perpendicular to the long diagonal of the diamond. For each filling, the C_{3z} symmetry is spontaneously broken, and $C_{2z}T$ is preserved, allowing Dirac points away from high symmetry points of the moiré Brillouin zone. The first panel for $n = 0$ is also shown in the main text Fig. 1(C). (B) The non-interacting band structure of tBLG calculated using the continuum model (without interaction), and plotted along the moiré Brillouin zone high symmetry lines shown in the top insert of (B). The lowest 8 bands are connected among each other by Dirac points, and are gapped from higher bands, which is different from the Hartree-Fock interacting band structures in (A). All the bands presented here are 4 fold degenerate.

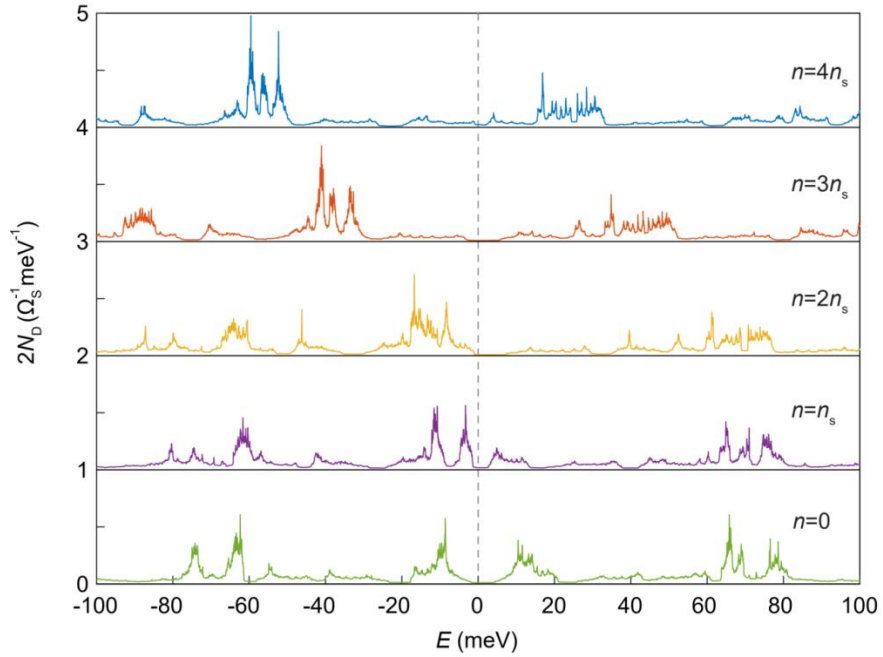


Fig. S11. Density of states in 0.45° tBLG continuum model with Coulomb interactions between electrons considered using the Hartree-Fock method at zero magnetic field, where we assume no spin or valley degeneracy breaking. The calculations are done for full moiré band fillings $n = Nn_s$. The corresponding Hartree-Fock band structures are shown in Fig. S10A. Note that the energy values shown in x axis are relative to the Fermi energy values which are all set at zero (indicated by the grey dashed line).

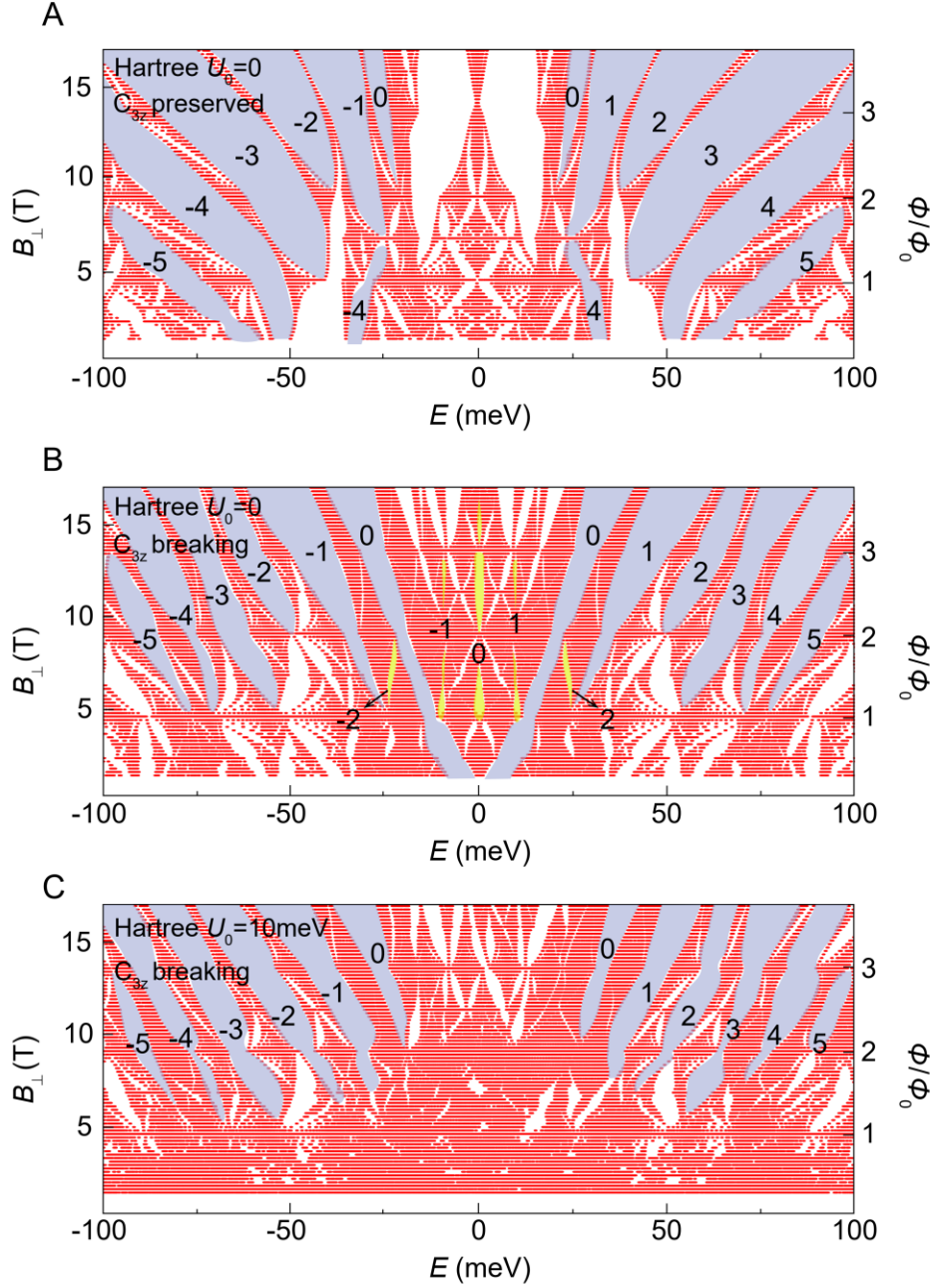


Fig. S12. Calculated Hofstadter Butterfly of 0.45° tBLG. Hofstadter butterfly of the tBLG continuum model (one-spin one-valley) under different Hartree potential and C_{3z} configurations. In (B) and (C), a 0.4% strain is considered and C_{3z} symmetry is broken by a single particle term. A 10meV Hartree potential is further considered in (C). $C = \pm 4$ gaps are highlighted with light blue color with corresponding numbers denoting different s values. Yellow color in (B) highlights $C=0$ gaps ($s = 0, \pm 1, \pm 2$) which reappear at high B_{\perp} field ($\phi > \phi_0$).

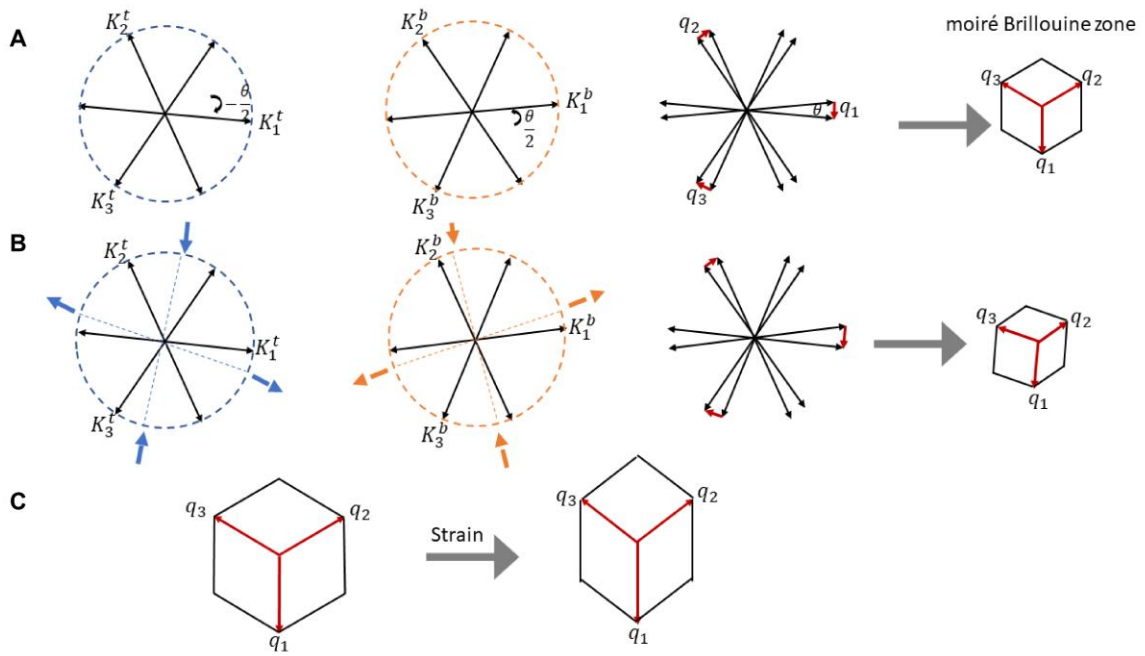


Fig. S13. Strained tBLG. (A) Momentum space of tBLG without strain. The momentum space of top layer of graphene rotated by $-\frac{\theta}{2}$ and bottom layer rotated by $\frac{\theta}{2}$. The momentum difference of the Dirac points of the two layers is used to construct the moiré Brillouin zone. (B) The rotated top and bottom layers are under independent uniaxial strain. The resultant momentum difference between the Dirac points are no longer related by C_{3z} rotation symmetry. (C) The specific choice of strained moiré Brillouin zone used in the Hofstadter butterfly calculations.

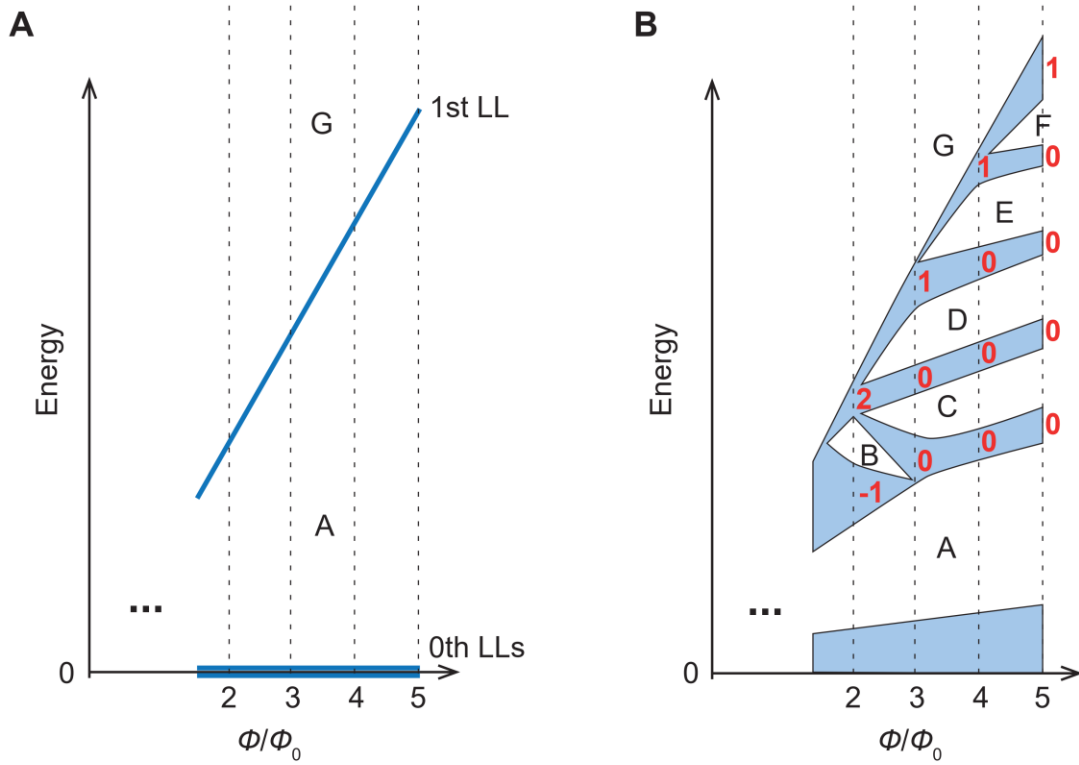


Fig. S14. (A) Illustration of the LLs in the untwisted bilayer graphene at nonzero magnetic field. Counting the 4-fold spin-valley degeneracy, the LL gap A carries Chern number $C = 4$, and the LL gap G has Chern number $C = 8$. At zero magnetic field, all the LL gaps collapse to the CNP. (B) Illustration of large magnetic field Hofstadter butterfly of twisted bilayer graphene, which can be viewed as the LLs of the untwisted bilayer graphene splitting into moiré subbands, during which we assume the LL gaps of untwisted bilayer graphene (e.g., A and G) remain open (above certain threshold magnetic field). ϕ/ϕ_0 is the number of magnetic fluxes per moiré unit cell. For illustration purpose, only the splitting of the 1st LL is shown, while the splitting of the 0th LLs (per spin per valley) are not shown. The red numbers near the dashed vertical lines denote the Chern number σ_j of the subbands (per spin per valley) at integer magnetic fluxes (the dashed vertical lines).

SI References

1. Z. Song et. al., All “Magic Angles” Are “Stable” Topological. *Phys. Rev. Lett.* 123, 36401 (2019).
2. B. Lian, F. Xie, B. A. Bernevig, Landau level of fragile topology. *Phys. Rev. B* 102, 1–7 (2020).
3. H. C. Po, H. Watanabe, A. Vishwanath, Fragile Topology and Wannier Obstructions. *Phys. Rev. Lett.* 121, 126402 (2018).
4. J. Herzog-arbeitman, N. Regnault, B. A. Bernevig, Hofstadter Topology: Non-crystalline Topological Materials at High Flux. *Phys. Rev. Lett.* 125, 236804 (2020).
5. Y. Jiang et al., Charge order and broken rotational symmetry in magic-angle twisted bilayer graphene. *Nature.* 573, 91–95 (2019).
6. Y. Xie et. Al., Spectroscopic signatures of many-body correlations in magic-angle twisted bilayer graphene. *Nature.* 572, 101–105 (2019).
7. Y. Choi et al., Electronic correlations in twisted bilayer graphene near the magic angle. *Nat. Phys.* 15, 1174–1180 (2019).
8. A. Kerelsky et al., Maximized electron interactions at the magic angle in twisted bilayer graphene. *Nature.* 572, 95–100 (2019).
9. S. Carr, S. Fang, Z. Zhu, E. Kaxiras, Exact continuum model for low-energy electronic states of twisted bilayer graphene. *Phys. Rev. Res.* 1, 1–6 (2019).
10. S. Fang et al., Angle-Dependent $\{ \text{Ab initio} \}$ Low-Energy Hamiltonians for a Relaxed Twisted Bilayer Graphene Heterostructure, arXiv:1908.00058 (2019).
11. R. Bistritzer, A. H. MacDonald, Moiré bands in twisted double-layer graphene. *Proc. Natl. Acad. Sci. U. S. A.* 108, 12233–12237 (2011).
12. H. C. Po et. al., Faithful tight-binding models and fragile topology of magic-angle bilayer graphene. *Phys. Rev. B.* 99, 195455 (2019).
13. B. A. Bernevig, T. L. Hughes, S.-C. Zhang, Quantum spin Hall effect and topological phase transition in HgTe quantum wells. *Science* (80-.). 314, 1757–1761 (2006).